ANALYSIS OF ELECTRON PRECIPITATION FROM AURORAL OPTICAL AND RADAR DATA MEASURED DURING DIFFERENT TYPES OF PULSATING AURORA

COMBINED EXTERNAL INTERNSHIP AP - NF; 3APNF15; 15 ECTS

UNIS
The University Centre in Svalbard

AUTHOR

D.A.J. VOGELS (1474936) - APPLIED PHYSICS & NUCLEAR FUSION

UNIS SUPERVISOR

PROF. NOORA PARTAMIES

THE UNIVERSITY CENTRE IN SVALBARD
DEPARTMENT OF ARCTIC GEOPHYSICS
SPACE PHYSICS

TU/E SUPERVISOR & EXAMINERS

DR. IR. HJALMAR MULDERS
DR. JURGEN KOHLHEPP

EINDHOVEN UNIVERSITY OF TECHNOLOGY
DEPARTMENT OF APPLIED PHYSICS
ELEMENTARY PROCESSES IN GAS DISCHARGES

MAY 5, 2025

THE UNIVERSITY CENTRE IN SVALBARD

Contents

Executive summary

This study explores the electron precipitation spectra related to the different subtypes of pulsating aurora (PsA), Amorphous Pulsating Aurora (APA), Patchy Pulsating Aurora (PPA), and Patchy Aurora (PA), using observations from the European Incoherent Scatter Radar (EISCAT) and Polar Orbiting Environmental Satellites (POES). By analyzing electron density profiles and differential electron fluxes, clear differences in electron precipitation energies and atmospheric penetration depths were identified among PsA subtypes. APA events were found to peak at higher altitudes around 109 km, while PPA and PA penetrated deeper, approximately between 104 and 106 km, consistent with spectral hardening and elevated electron energies. A significant shift towards higher-energy precipitation, spectral hardening, occurred around 23 magnetic Local Time (MLT), particularly evident in PPA events. However, data from POES satellites, despite their broader spatial coverage, did not clearly separate the PsA subtypes, highlighting the limitations inherent to spatially averaged satellite observations. These results indicate that the morphological differences among PsA subtypes are rooted in varying magnetospheric chorus wave interactions and electron source dynamics, reinforcing the value of employing a multi-instrument approach to unravel the complexity of pulsating auroras. However, due to the limited number of analyzed events, the findings presented here should be considered preliminary. A continuation of this study with larger datasets would be needed to conclusively confirm these subtype differences.

1 Introduction

Auroras are natural light phenomena that illuminate the polar skies with a vibrant display of colours. They are the result of complex interactions between solar wind particles and Earth's magnetosphere. Energetic electrons spiral along magnetic field lines and collide with gases in the upper atmosphere; these collisions excite atmospheric atoms and molecules, causing them to emit visible light, which can be observed as structured arcs and ribbons of discrete auroras. A less understood and more dynamic phenomenon is known as pulsating aurora (PsA). These consist of diffuse flickering patches that switch on and off with quasi-periodic timing on the scale of 2-20 seconds [1].

PsA usually occurs during the recovery phase of substorms, which occur in the post-midnight to early morning hours, but can also appear during the expansion phase [2]. PsA is believed to be the result of wave-particle interactions, specifically lower-band chorus waves and plasma sheet electrons injected into the inner magnetosphere during geomagnetic activity [3]. This can result in the precipitation of electrons ranging from 10 keV to several hundred keV, capable of reaching $\sim$68 km and affecting mesospheric chemistry [4].

More recent studies theorize that PsA is not a uniform phenomenon but has distinct subtypes. These three subtypes are Amorphous Pulsating Aurora (APA), Patchy Pulsating Aurora (PPA), and Patchy Aurora (PA); each has its own characteristics, which set it apart:

1. APAs are structureless diffuse emissions with rapid, irregular pulsation that constantly changes. These are the most commonly observed subtype [5].
2. PPAs are coherent, well-defined patches with regular pulsation across their area. These structures often have convection flow drift and can last for minutes at a time, which points to magnetospheric drivers [6].
3. PAs resemble PPA in structure, but lack any significant pulsation. Despite the difference with PPA, it is believed that they originate from similar precipitation mechanisms, with, if present, modulation below visibility thresholds [7].

Statistical analyses of over 400 PsA events have shown that PsA events have a median duration of 1.4 hours, and many events end only due to observational limitations. PsA often emerges from pre-existing, less-energetic auroral conditions dominated by diffuse precipitation [8]. At the onset of PsA, peak auroral emission heights typically drop by about 8 km, indicating a transition to more energetic precipitation [2]. Patch size evolution during PsA has been shown to be not uniform: patches often shrink during recovery phases and expand during substorm expansion, insinuating different underlying magnetospheric processes [6].

In this study, the aim is to get a better understanding of the behaviour of PsA subtypes in terms of the precipitation energy through differential electron flux. The different subtypes of pulsating aurora will be observed using Polar Orbiting Environmental Satellites (POES) and the European Incoherent Scatter Aktiebolag (EISCAT AB), formerly known as the EISCAT Scientific Association, radar system, which is located in Tromsø, Norway (69.9°N, 19.2°E). In addition, this also evaluates how effectively the POES satellite and EISCAT radar techniques capture and distinguish the differential electron flux features of each PsA subtype.

PsAs are not just interesting from a space physics perspective, but also because of its possible effects on the atmosphere. The energetic electrons involved in PsA can reach down to altitudes around 70 to 100 km, where they cause ionisation. This process leads to the production of odd nitrogen (NO_x) and hydrogen species (HO_x), which can break down ozone in the polar regions [9, 4]. Since PsA is a common and long-lasting phenomenon that also shows up during relatively quiet geomagnetic conditions, it might actually play a bigger role in long-term changes in atmospheric chemistry than we previously thought. While this study aims to enhance that understanding, it is based on relatively small datasets and should thus be viewed as more of an exploration of subtype differences.

POES data offers a broad spatial coverage of electron precipitation fluxes, by cross-examining the time and location of the satellites with the keograms of the Magnetometers-Ionospheric Radars-All-sky Cameras Large Experiment (MIRACLE) network and a list of PsA events, the electron precipitation fluxes during different subtypes of PsA events can be found.

From EISCAT radar data electron density profiles, altitudes of ionization, differential electron flux spectra, and more can be derived. Analyzing this data will provide a better understanding of the PsA subtypes. Although total energy flux can also be derived, this study focuses on the differential spectra.

2 Methodology

This study employs a multi-instrumental approach to analyze the energetic and spatial characteristics of different PsA subtypes. Data from POES and the EISCAT radar system are used to examine the characteristics of these subtypes. While both approaches yield estimates of electron energy spectra, they capture different stages of the precipitation process and differ significantly in spatial and temporal resolution.

2.1 Ground-Based Electron Energy Spectrum Retrieval (EISCAT)

One of the approaches to investigating the characteristics of precipitating electrons during different subtypes of PsA involves electron density profiles derived from the EISCAT radar systems, specifically Ultra High Frequency (UHF), 931 MHz, radars, the geographical location of the EISCAT UHF is given in figure 1. These profiles can be used to infer the energy spectra of the electron precipitation responsible for the PsA in the ionosphere.

2.1.1 Electron Density Profiling

For this study, data from publicly available field-aligned EISCAT experiments were used. While specific parameters such as temporal resolution may vary between experiments, all datasets share the critical characteristic of having been recorded in a field-aligned configuration, ensuring consistency in the measurement geometry. The field-aligned radar configuration provides electron density measurements with a beam width of approximately 0.6°, yielding a horizontal spatial resolution of around 1 km at an altitude of 100 km [10], and the vertical resolution is typically 3-6 km. These measurements were then analysed using Grand Unified Incoherent Scatter Design and Analysis Package (GUISDAP) software. GUISDAP derives the electron density and other plasma parameters, such as electron and ion temperatures and ion velocity, by fitting the theoretical incoherent scatter spectrum to the observed autocorrelation functions (ACFs) of the backscattered radar signal. This inversion takes known instrument parameters and ionospheric conditions into account, such that it provides physically meaningful estimates of the ionospheric plasma state [11].

2.1.2 Inversion to Electron Flux Spectra with ELSPEC

To derive the electron flux spectra, the Electron Spectrum (ELSPEC) inversion algorithm [12] was used on the electron density profiles. The ELSPEC inversion algorithm integrates the electron continuity equation;

$$\frac{\delta n}{\delta t} = Q - \alpha n^2,$$

where n is the electron number density, Q is the ionization production rate and α is the effective recombination coefficient. To avoid amplification of noise in time derivates ELSPEC uses an analytic integration of the continuity equation. The system then selects an optimal spectrum shape using the Akaike Information Criterion [13]. Effective recombination rates are determined from composition of ion species using the International Reference Ionosphere (IRI) model, the IRI model is an empirical standard model of the Earth's ionosphere, developed through international collaboration and is maintained under the Committee on Space Research (COSPAR) and the International Union of Radio Science (URSI). The IRI model provides information such as electron density, electron and ion temperatures and ion composition as functions of location, altitude, time of day, season, and solar / magnetic activity [14]. Lastly, the altitude-dependent ion production rates are calculated using the Fang et al. (2010) model as a function of electron energy, altitude, and atmospheric composition [15]. The atmospheric composition is found via the Naval Research Laboratory Mass Spectrometer and Incoherent Scatter Radar Extended model - 2000 (NRLMSiSE-00), which is an empirical atmospheric model developed by the U.S. Naval Research

Laboratory (NRL). It provides estimates of the composition, temperature and density of Earth's atmosphere from the surface up to a 1000 kilometres [16].

The differential number flux $I(E)$ as a function of electron energy is estimated and used directly for analysis through this method. It will be used to better understand the different subtypes of PsA events. While the ELSPEC algorithm allows for transformation into the differential energy flux or total energy flux, this study focuses on the unconverted differential number flux.

2.2 Satellite-based electron flux measurements (POES)

The National Oceanic and Atmospheric Administration (NOAA) POES constellation operates on lower earth orbit (∼850 km) and it carries two particle detectors: Total Energy Detector (TED) and Medium Energy Proton and Electron Detector (MEPED), which perform in-situ measurements of precipitating electrons at overpass altitude [17]. This will give us a snapshot of the unfiltered electron energy distribution before atmospheric interaction. Another aspect to take into account is that POES sampling is limited in both time and space. Each satellite only has a narrow path and measurements are averaged over regions spanning up to hundreds of kilometres.

The TED and MEPED detectors allow for in-situ characterization of the precipitating electron energy spectra during PsA events, providing discrete flux measurements across defined energy channels. TED supplies differential fluxes across channels spanning 0.19, 0.84, 2.6 and 7.9 keV, while MEPED provides integral flux measurements at 43, 114, 292 and 756 keV [9].

Flux measurements from the 0° telescopes, oriented along the local magnetic field line, were used to isolate the electrons that have the highest chance of precipitating into the ionosphere. These fluxes are reported in units of $\mathrm{cm}^{-2}\ \mathrm{s}^{-1}\ \mathrm{sr}^{-1}\ \mathrm{keV}^{-1}$, where the term sr^{-1} refers to steradian. A steradian is the SI unit of a solid angle. Since electrons arrive from all directions in space, using steradians allows the detectors to normalize flux per unit solid angle. This makes it possible to compare directional measurements. This is very important for instruments like MEPED, MEPED measures electrons coming from specific angles relative to the magnetic field. These directional flux measurements are essential for accurately capturing the characteristics of precipitating electrons and understanding wave-particle interactions during PsA events.

Unlike Tesema et al. (2020) [9], no power-law fits were used to construct a generalized energy spectrum across a large dataset of events was used. The analysis used in this paper is based on eight energy bins. Given the limited number of bins and events, the aim was to preserve the shape and variability of the observed spectra. This approach focuses on the structural features of individual events.

2.2.1 MIRACLE network and Keograms

To help with categorizing the PsA subtypes, ground-based optical data from the MIRACLE network was used. MIRACLE is a network of several all-sky cameras located across northern Scandinavia, the stations used in this study are: Kilpisjärvi (KIL), Kevo, (KEV), Abisko (ABK), Sodankylä (SOD) and Muonio (MUO); their geographical locations are given in figure 1. These cameras provide continuous wide-angle views of auroral activity, which is essential for capturing the morphology and timing of PsA.

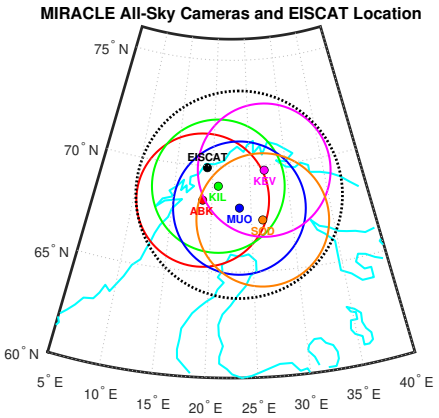

Figure 1: *Geographic locations of the MIRACLE network all-sky cameras used in this study and the EISCAT AB UHF radar.*

Using the all-sky camera, keograms were created. A keogram is a time-series image showing auroral intensity along a fixed line across the sky, in this case from north to south, stacked over time. From this we get a clear view of how auroral features move and evolve. By visually inspecting the keograms during satellite overpass times, we could classify events as APA, PPA, or PA based on their structure and pulsating behaviour.

2.2.2 Data analysis

To analyze the differences between the PsA subtypes, a list of ∼2000 PsA events within northern Scandinavia was cross-referenced with satellite overpass data. This produced a list of approximately 250 uncategorized PsA events that coincided with an overpass. The satellite ground tracks were mapped onto the field of view of the MIRACLE Network with the timing of the overpass, this is shown in figure 2a. Then each event was manually analyzed using the keograms corresponding to the overpass time, as shown in figure 2b. SKN in figure 2a refers to Skibotn, which is another all-sky camera which is not part of the MIRACLE network. On the basis of the spatial and temporal auroral characteristics observable in these keograms, the PsA subtype could be found. For example, looking at the timespan given in figure 2a within figure 2b shows us a clear patchy aurora. Due to the strict criteria, the number of events that were analyzed are limited, only 35. As such the statistical interpretation of the differences between the subtypes is constrained by the smaller sample size.

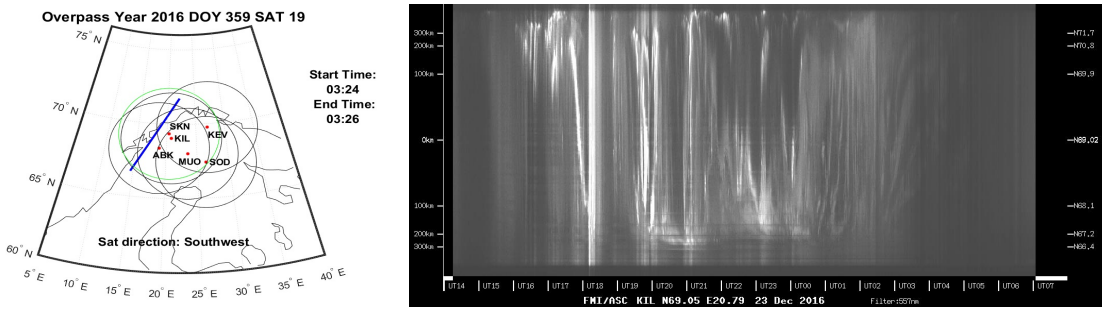

(a) *Satellite overpass information and MIRACLE network*

(b) *Keogram from the Kilpisjärvi EMCCD camera*

Figure 2: *The manual categorization process*

3 Theory

3.1 Fundamentals of Auroral Physics

Auroras are luminous displays that occur in the upper atmosphere, typically between 80 and 500 km altitude. This results from interactions between charged particles from the solar wind and Earth's magnetosphere [18, 8]. When solar wind particles enter the magnetosphere, as schematically shown in figure 3, they are led by Earth's magnetic field toward the polar regions. These electrons will collide with atmospheric gases such as molecular nitrogen and atomic oxygen as they precipitate into the ionosphere. These collisions excite these atoms and molecules, which consequently release photons upon returning to their ground state, producing visible auroral emissions. The colour and altitude of these emissions change depending on the energy of the electrons and the type of gas involved. Green auroras, the most common, are typically produced by atomic oxygen at altitudes of 100-150 km. Red emissions from atomic oxygen usually occur at altitudes above 200 km. Finally, blue and violet hues are generally associated with nitrogen and occur at lower altitudes.

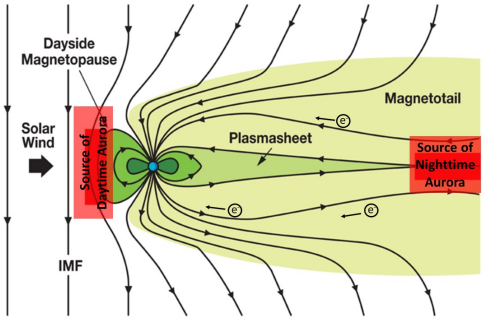

Figure 3: *Schematic of the interaction between the Interplanetary Magnetic Field (IMF) and Earth's magnetosphere [19].*

Auroral activity is concentrated in two ring-shaped zones, called auroral ovals, around the magnetic poles, a schematic of the auroral oval is shown in figure 4. These ovals are the regions where auroras are most likely to occur and the area expands or contracts depending on geomagnetic activity [20]. The auroral oval is maintained by the coupling between the solar wind, the ionosphere and the magnetosphere, and it changes in local time and latitude as a response to solar wind pressure and the interplanetary magnetic field orientation.

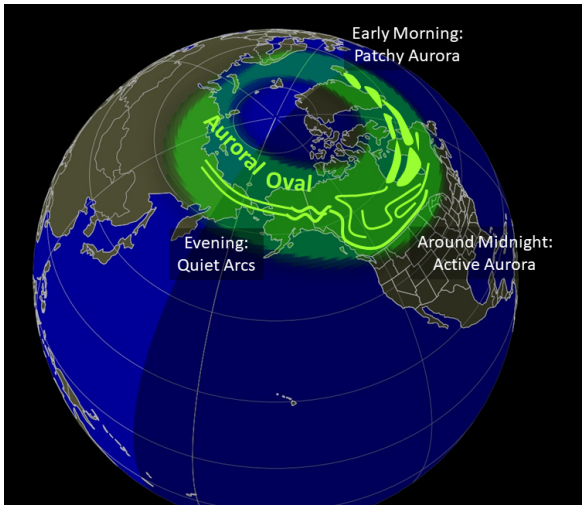

Figure 4: *Schematic of an auroral oval [19].*

One very important source of auroral precipitation is the plasma sheet, this is a region in the magnetotail of Earth's magnetosphere where hot, weak plasma accumulates, this area is also shown within figure 3. The magnetotail acts as a reservoir for energetic electrons and ions. During geomagnetic disturbances, like substorms, particles from the plasma sheet are injected earthward, which leads to enhanced auroral activity [21].

Substorms are transient, large-scale reconfigurations of the magnetosphere that occurs in three phases: the growth phase, where energy from the solar wind is stored in the magnetotail; the expansion phase, where the stored energy is quickly released; and the recovery phase, during which auroral activity gradually wanes and the system returns to a quieter state [21, 18].

Auroras can be classified into diffuse and discrete types. Discrete auroras appear as structured arc, bands and patches that can change in shape and brightness rapidly, while diffuse auroras are more uniform and faint, usually forming the background to discrete auroras [8]. PsA is considered a subtype of diffuse aurora. Even though PsA may appear patchy and dynamic, it lacks the well defined spatial structures typical of discrete aurora. Furthermore, PsA is not generated by field-aligned electric potentials, but rather by isotropic electron precipitation caused by wave-particle interactions [22]. Lastly, PsA occurs during the substorm recovery phase, and its location in the equatorward portion of the auroral oval places it firmly within the diffuse aurora category.

3.2 Physical Mechanisms of Pulsating Aurora

As explained earlier, a pulsating aurora is a diffuse auroral phenomenon generated by wave-particle interactions in the Earth's magnetosphere. PsA originates from pitch-angle scattering of magnetospheric electrons into the atmospheric loss cone by magnetospheric waves, which then results in interactions with atmospheric gases.

PsA occurs primarily during the recovery phase of substorms, when the plasma sheet is still active but field-aligned acceleration mechanisms, which drive discrete aurora, have subsided. At that stage, electrons from the nightside plasma sheet and the outer radiation belt are injected into the upper magnetosphere, to be more specific in the post-midnight to dawn, 01 to 06 magnetic local time (MLT). MLT is a timekeeping system that is typically used in space and geophysics to describe the position of the Sun relative to Earth's magnetic field, so 12 MLT corresponds to the position directly facing the Sun along Earth's magnetic field lines and 00 MLT refers to the exact opposite, magnetic noon and midnight, respectively [23]. Looking at figure 4, MLT 00 would be on the right side and MLT 12 on the left side. In Tromsø MLT is Universal Time (UT) + 2.5. The conditions from

post-midnight to dawn are favourable for the growth of whistler-mode chorus waves. These are the waves that drive the scattering and the resulting PsA events [1, 3, 22].

The precipitating electrons during PsA typically have an energy range between 10 to 200 keV, which makes it possible to reach atmospheric altitudes (70-90 km). This energy deposition into the upper atmosphere produces both visible aurora and measurable ionization [4, 9].

3.3 Whistler-Mode Chorus Waves

Whistler-mode chorus waves are a type of very low frequency (VLF) electromagnetic wave found in the Earth's magnetosphere. They are called "whistler-mode" because of the way they travel along field lines and their similarity to early radio wave detections of lightning, which produced a "whistling" sound in recordings. These waves form naturally when energetic electrons become unstable, specifically when there is a temperature anisotropy. Temperature anisotropy is when the perpendicular velocity of electrons is higher than the parallel velocity relative to the field lines. These waves are usually generated near the equator [3].

These chorus waves exist in two frequency bands; lower and upper band. The lower band has a frequency between 0.1 and 0.5 times the local electron cyclotron frequency (ECF) and is most effective in scattering electrons into the loss cone. The upper band has a frequency greater than 0.5 times the local ECF. Although it can interact with particles, it is not as effective for PsA precipitation [3].

These waves grow in discrete bursts with time scales of several seconds [24]. This matches the quasi-periodic pulsation cycles seen in PsA. Chorus waves interact with electrons across a large energy range through cyclotron resonance, inducing pitch-angle scattering and directing those electrons into the atmosphere. These interactions not only cause the precipitation but also modulate the intensity, which explains the pulsating behaviour of PsA observed through all-sky cameras [24, 25].

Chorus wave activity is strongly dependent on MLT, with peak occurrence between 01 and 06 MLT, this is the same region as where PsA is most frequently observed [2]. The structures and coherence of chorus wave packets can influence whether the resulting PsA appears as structured, periodic patches or as amorphous, irregular emissions [24, 25].

3.4 Characteristics and subtypes of PsA

Although the subtypes of pulsating aurora - APA, PPA and PA - have been well defined in recent literature, their importance extends beyond morphological categorization [7]. These subtypes most likely represent variations in the underlying wave-particle interaction dynamics, precipitating electron energies and temporal coherence of magnetospheric chorus wave activity [5, 6, 7].

Each subtype can be connected to distinct ionospheric and magnetospheric conditions. First of all, APA is more associated with lower-energy and more isotropic electron precipitation, which results in ionization to peak at higher altitudes, around 110 km, and it lacks a strong modulation signature. Secondly, PPA reflects more coherent interactions between the electrons and chorus wave bursts. As a result, a more structured and periodic modulation of precipitation can be observed. The peak ionization usually occurs around 105 km and occasionally can even extend as low as 70 km. Lastly, PA is theorized to stem from mechanisms similar to PPA but lacks visible modulation. PA also peaks near 105 km, although overall ionization tends to be weaker than PPA [26].

These differing penetration depths and spatial structures reflect the differences in precipitation energies for the subtypes of PsA: APA is linked to tens of keV, while PPA and PA can even involve electrons up to 200 keV. These energy levels directly influence the penetration depth of the electrons and, as such, also the ionization altitude. This gives a clear physical distinction between the subtypes [26].

In Tesema et al. (2020) it is also stated that PPA has a thicker ionization layer compared to PA. This is theorised to be due to the fact that PPA has a broader electron energy range compared to PA [26].

In addition to structural and energetic differences, the PsA subtypes also show distinct occurrence patterns in relation to the magnetic local time (MLT). Figure 5 from Grono and Donovan (2020) provides valuable information on the temporal occurrence patterns of the three subtypes of PsA as a function of magnetic latitude (MLAT), based on 10 years of all-sky camera data.

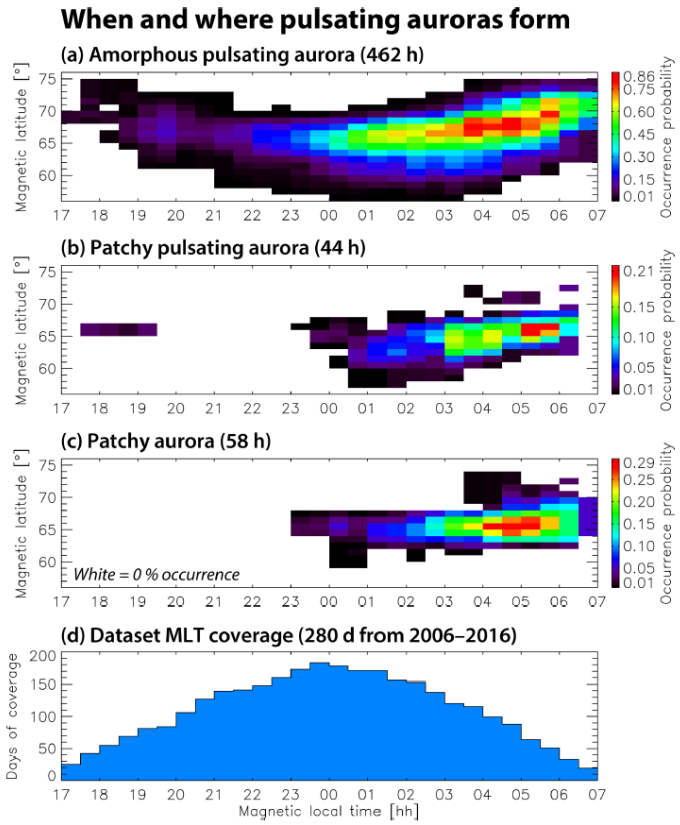

Figure 5: *Occurrence probability of pulsating auroras based on a survey of times when Rankin Inlet, Gillam, and Pinawa THEMIS ASI had good visibility between 2006 through 2016. White bins in panels (a), (b), and (c) have data coverage but no events, corresponding to a 0% occurrence probability. Panel (d) shows the number of days of data that had clear visibility in each MLT bin and coverage is uniform across the MLAT bins [5].*

Figure 5 shows a clear separation in when and where each subtype would typically appear. APA is extremely common; it occurs daily between 23 and 07 MLT, and beyond, with a wide latitudinal spread. PPA is comparably less frequent, PPA occurs mainly between 03 and 06 MLT, but can happen at other times as well. Finally, PA appears in a temporal range similar to that of PPA but displays a smaller latitudinal band.

These patterns lead to the idea that APA dominates in the early phase of PsA activity and that PPA and PA become more present in the early morning sector, consistent with the evolution of magnetospheric wave activity.

The classification into subtypes serves as a bridge between ground-based auroral observations and the magnetospheric processes that drive them. It also enables more systematic comparisons of energy deposition altitudes, differential electron flux patterns, and the spatial-temporal evolution

of auroral patches, providing insight into how differences in chorus wave structure and amplitude manifest themselves in the ionosphere.

4 Results & Discussion

4.1 Analysis of EISCAT radar data

EISCAT radar data was gathered for 47 PsA events; 22 APA, 19 PPA, and 6 PA events. In order to validate the found data, some of the data was plotted and compared with characteristics found in previous papers.

In Tesema et al. (2020) the median altitude at which the different PsA types have their maximum electron densities has been shown. For APA the altitude is at ∼110 km, for PPA it is generally below 105 km and sometimes reaching 95 km, and PA is similar to PPA [26].

To describe these changes, the term spectral hardening is used to refer to a shift toward higher-energy electron precipitation, which is visible as an increase in flux at the upper end of the energy spectrum. As a consequence, the altitude of the maximum electron density is expected to lower, which is referred to as deeper penetration into the atmosphere. These terms are used throughout the analysis to distinguish between the shape of the electron spectrum and the altitude at which its effects are observed.

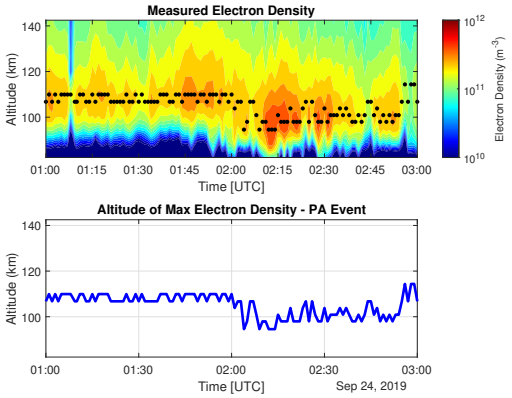

(a) *Heatmap of electron density over time and altitude for a single PsA event. The scatterplot dots indicate the altitude at which the maximum electron density occurs at each time step. The lower panel shows this altitude over time as a line plot.*

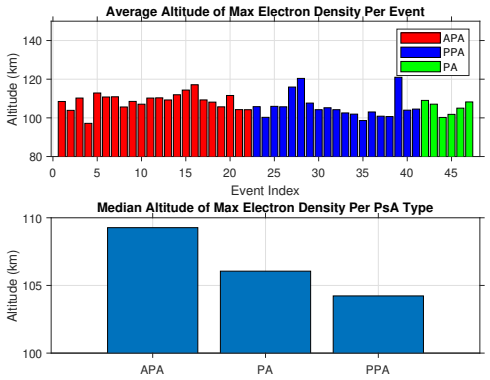

(b) *Histograms showing (top) the time-averaged altitude of maximum electron density per event and (bottom) the median altitude per PsA subtype.*

Figure 6: *Altitude of maximum electron density during PsA events, derived from EISCAT radar data.*

4.1.1 Differential Electron Flux Analysis

In figure 6a, the electron density is shown as a function of altitude and time for a single PsA event. For each point in time, the altitude where the maximum electron density occurs is marked by a scatterplot dot. This altitude is then averaged over time for every event, which results in the values shown in the upper subplot of figure 6b. The median altitudes of the maximum electron density per PsA subtype can then be found, and are also shown in the lower subplot of figure 6b. APA comes in at around 109 km, while PA and PPA are found at 106 km and 104 km, respectively. These values are slightly different from those mentioned in Tesema et al. (2020), but that could be due to the smaller sample size used here [26].

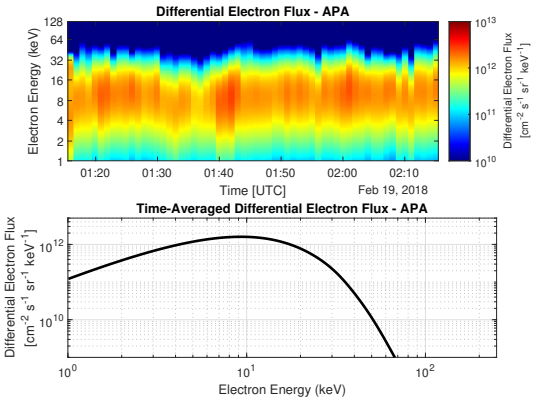

(a) *Heatmap of (top) the differential electron flux over time and electron energy for a single APA event and (bottom) time-averaged differential electron flux of the same event, plotted over electron energy.*

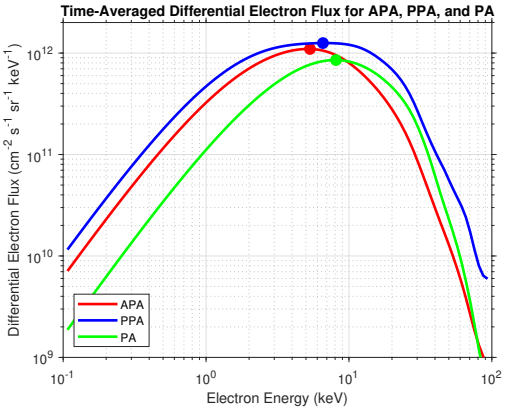

(b) *Time-averaged differential electron flux as a function of electron energy, averaged over all events per PsA subtype.*

Figure 7: *Event-specific and subtype-averaged differential electron flux profiles, based on EISCAT radar data.*

To explore the characteristics of the PsA subtypes in more detail, the time-averaged electron flux was plotted, first for every event which is shown in figure 7a. Afterwards the time-averaged electron flux per PsA subtype was plotted in figure 7b. Some things become quite clear quite quickly. For instance, PA and PPA both have more high energy electrons compared to APA, which explains the deeper penetration into the atmosphere observed in those subtypes. The figure also offers additional insight into the ongoing discussion between Yang et al. (2019) [27] and Tesema et al. (2020) [26] regarding the relative energy ranges of APA and PPA. Whereas Yang suggests APA has a higher energy range, the results shown here support Tesema's findings instead.

4.1.2 The influence of MLT

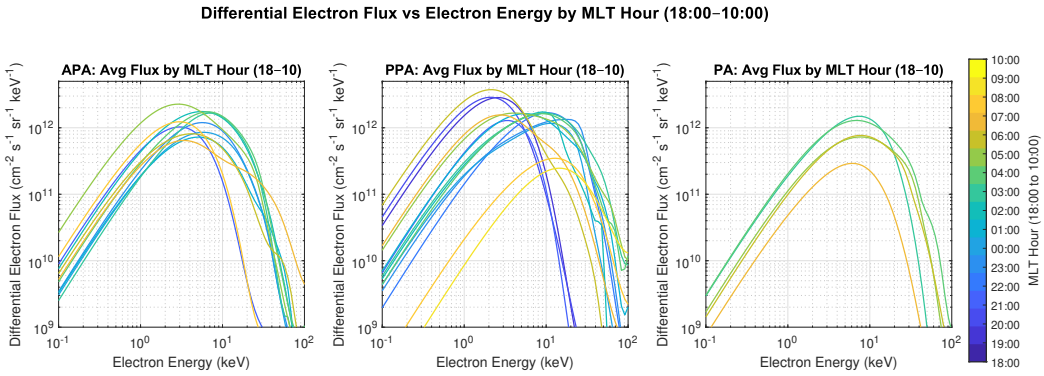

Figure 8: *Subtype-averaged evolution of the differential electron flux as a function of electron energy across MLT, derived from EISCAT radar data.*

An aspect that has not yet been discussed in relation to electron flux is the influence of MLT. Figure 8 shows the average differential electron flux versus energy across MLT hours, separated by PsA subtype. Grono et al. (2020) already outlined general occurrence windows per subtype,

which are largely reflected in our data. A clear shift to higher energy is visible around 23 MLT in the electron energy spectra, especially for APA and PPA, indicating spectral hardening at this time. However, after approximately 07–08 MLT, the differential electron flux begins to decrease, suggesting a weakening of precipitation as the magnetospheric driving conditions diminish. For APA, spectral hardening around 23 MLT is present but less pronounced than for PPA. In the case of PA, no clear MLT-dependent shift is observed, likely due to the absence of events before 01 MLT and a limited sample size.

One striking feature is the peak in PPA flux around 18–19 MLT. Although PsA is typically associated with the recovery phase of substorms and thus more common after midnight, this early PPA activity suggests that under certain magnetospheric conditions, such as a particularly active plasma sheet during the substorm expansion phase, chorus wave generation may begin earlier. Figure 5 also shows these early evening PPA auroras. The gap in activity following this peak until around 23 MLT could indicate a transitional phase where wave–particle interaction conditions are not yet optimal for sustained PsA. The resurgence in precipitation after 23 MLT aligns with increased lower-band chorus wave activity in the post-midnight sector, as described in the theory section. These chorus waves are more structured and intense between 01 and 06 MLT, matching the timing of the observed spectral hardening and corresponding deeper penetration into the atmosphere, especially for PPA. The evolving chorus wave intensity and structure modulate the resonance conditions for pitch-angle scattering, resulting in the time-dependent flux variations seen across all subtypes.

Even APA, which is typically linked to more isotropic and lower-energy precipitation, shows spectral evolution over MLT, indicating that the underlying electron source population, likely from the plasma sheet, is also dynamic. Slightly harder injections later in the night or subtle increases in chorus wave coherence can enhance the high-energy contribution in APA, particularly near the APA–PPA transition region. These findings support the interpretation that all PsA subtypes are embedded within an evolving magnetospheric environment where the interplay between chorus waves, plasma sheet injections, and resonance conditions drives both the timing and characteristics of auroral precipitation.

4.2 Analysis of POES data

4.2.1 Differential Electron Flux Analysis

Of the 35 events that were measured using POES, 17 are APA, 8 PPA, and 10 PA. The resulting electron flux versus electron energy is plotted in figure 9a.

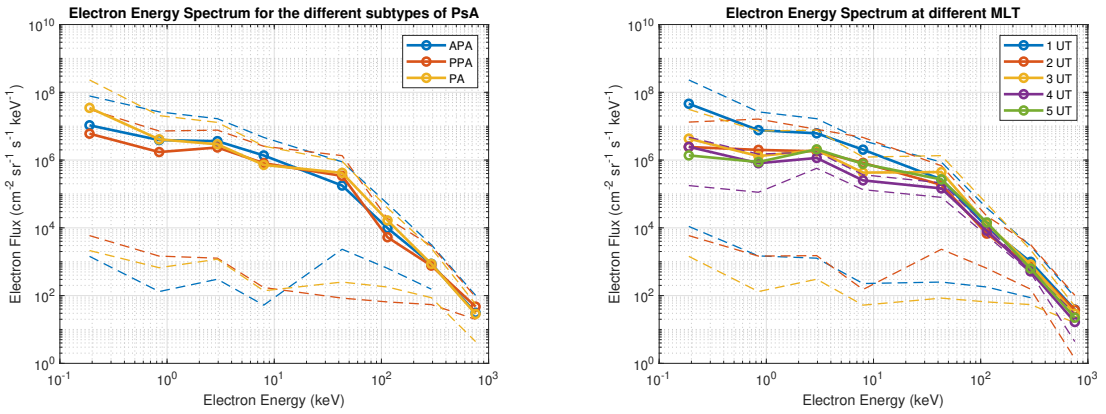

(a) *Electron flux as a function of electron energy, averaged over all events per PsA subtype.*

(b) *Electron flux as a function of electron energy across MLT.*

Figure 9: *POES-derived differential electron flux spectra, showing (a) subtype-averaged profiles and (b) spectral evolution across MLT.*

In contrast to what is shown in figure 7b, figure 9a, derived from in-situ POES satellite data, does not show a comparable separation between PsA types. The spectral shapes and energy ranges for APA, PPA and PA are quite similar across the sampled events. This suggests that the type-dependent differences observed in the EISCAT data are either too subtle or localized to be captured through the POES constellation.

4.2.2 The influence of MLT

Looking closely at the POES electron flux across MLT hours, shown in figure 9b, reveals a relatively stable flux across the high-energy electrons, throughout the 01-05 MLT range. However, low energy electron flux shows a distinct decrease between 01 and 02 MLT, after which there is a consistent but slow decrease in flux. This trend suggests that while wave-particle interactions sustain high-energy precipitation during the post-midnight sector, the amount of scattering for lower energy electrons decrease. This supports a picture where chorus wave interactions evolve over MLT to favour higher energy resonances or reflect a depletion of low-energy source populations in the plasma sheet.

4.3 Comparison between ground-based and satellite observations

Several key factors could influence the discrepancies between the two methods. Firstly, POES observations are spatially averaged along the track, which is displayed in figure 2a, and there is a limited pitch-angle coverage. Secondly, where POES detects the incoming electron population before atmospheric interaction, EISCAT captures the resulting ionospheric response. Thus, this can include many aspects such as energy loss, recombination, and secondary ionization. Third, EISCAT has a very high spatial and temporal resolution, which allows it to detect localized or transient structures that could be averaged out in the satellite data. Lastly, the EISCAT spectra are derived using the ELSPEC inversion algorithm, as explained in the methodology. It is important to note that ELSPEC fits idealized spectral shapes to the found electron density. This means that some features may be enhanced or suppresed depending on the assumptions the algorithm made. As such, the resulting flux profiles are meaningful estimates, but they do not represent direct measurements of the electron energy distribution.

Although both POES and EISCAT offer helpful insights about the precipitating electrons, both methods describe radically different aspects. EISCAT seems to be better suited for observing the

subtle and fast-changing nature of pulsating auroras. POES, on the other hand, is more ideal for characterizing broader precipitation trends on larger spatial scales.

5 Conclusions & Recommendation

This study looked at how the different PsA subtypes, APA, PPA, and PA, behave in terms of differential electron flux, using both POES and EISCAT radar data.

The EISCAT observations succesfully showed clear differences among subtypes. APA events, as expected, peak at higher altitudes, while PPA and PA show deeper penetration, consistent with spectral hardening and higher energy electron precipitation. This lines up well with what previous papers suggested. PPA shows the strongest high-energy component, suggesting that chorus wave interactions are more coherent and energetic during these events. PA is somewhat similar to PPA but lacks clear modulation. Even though PPA and PA can look alike in structure, the electron flux profiles tell a different story. PA has a far smaller energy range compared to PPA.

Something that stood out in this study is the shift in electron flux across MLT. Around 23 MLT there is a clear increase in high-energy electrons, especially for PPA and to some extent APA. After 07–08 MLT this drops off again. There's also a surprising peak around 18–19 MLT in PPA, which might point to some early activity during the expansion phase. This suggests that chorus wave conditions, which are usually strongest between 01 and 06 MLT, are not the only driver.

Evaluating the data gathered from POES and comparing it to the EISCAT radar data revealed that the POES data did not show the same separation between the PSA subtypes as in the EISCAT radar data. This could be due to multiple factors, but an important one is the difference between spatial resolution of the two methods. POES data is an average over tens, or maybe even hundreds, of kilometres instead of the 1 kilometre EISCAT radar data gives.

In short, the results show that APA, PPA and PA are not just different shapes in the sky, but actually reflect differences in the wave–particle interactions going on in the magnetosphere. The changes over MLT, the differences in energy, and the consistency with previous studies all point toward a bigger picture where chorus waves, plasma sheet injections and local conditions together shape what we see in the aurora.

The logical next step would be to expand the limited sample size. This could be done by expanding the list of verified pulsating aurora times with their subtype; another possibility is to use data from other high-latitude incoherent scatter radars, such as the one at Poker Flat, Alaska. This would allow for a better spatial coverage and potentially different geomagnetic conditions compared to Tromsø. More events and observations at different latitudes and MLT sectors will possibly allow for a statistical classification of PsA subtypes based on the spectral shape and penetration depth.

6 References

[1] M R Lessard. A Review of Pulsating Aurora. In *Auroral Phenomenology and Magnetospheric Processes: Earth And Other Planets*, pages 55–68. American Geophysical Union (AGU), 2012. ISBN 9781118670286. doi: https://doi.org/10.1029/2011GM001187. URL https://agupubs.onlinelibrary.wiley.com/doi/abs/10.1029/2011GM001187.

[2] N. Partamies, D. Whiter, A. Kadokura, K. Kauristie, H. Nesse Tyssøy, S. Massetti, P. Stauning, and T. Raita. Occurrence and average behavior of pulsating aurora. *Journal of Geophysical Research: Space Physics*, 122(5):5606–5618, 2017. ISSN 21699402. doi: 10.1002/2017JA024039.

[3] Richard M Thorne, Binbin Ni, Xin Tao, Richard B Horne, and Nigel P Meredith. Scattering by chorus waves as the dominant cause of diffuse auroral precipitation m-6. *Nature*, 2010. doi: 10.1038/nature09467.

[4] S. Oyama, A. Kero, C. J. Rodger, M. A. Clilverd, Y. Miyoshi, N. Partamies, E. Turunen, T. Raita, P. T. Verronen, and S. Saito. Energetic electron precipitation and auroral morphology at the substorm recovery phase. *Journal of Geophysical Research: Space Physics*, 122(6):6508–6527, 2017. ISSN 21699402. doi: 10.1002/2016JA023484.

[5] Eric Grono and Eric Donovan. Surveying pulsating auroras. *Annales Geophysicae*, 38(1):1–8, 2020. ISSN 14320576. doi: 10.5194/angeo-38-1-2020.

[6] Noora Partamies, Karl Bolmgren, Erkka Heino, Nickolay Ivchenko, Joseph E. Borovsky, and Hanna Sundberg. Patch Size Evolution During Pulsating Aurora. *Journal of Geophysical Research: Space Physics*, 124(6):4725–4738, 2019. ISSN 21699402. doi: 10.1029/2018JA026423.

[7] E Grono and E Donovan. Differentiating diffuse auroras based on phenomenology. *Annales Geophysicae*, 36(3):891–898, 2018. doi: 10.5194/angeo-36-891-2018. URL https://angeo.copernicus.org/articles/36/891/2018/.

[8] Yukitoshi Nishimura, Marc R. Lessard, Yuto Katoh, Yoshizumi Miyoshi, Eric Grono, Noora Partamies, Nithin Sivadas, Keisuke Hosokawa, Mizuki Fukizawa, Marilia Samara, Robert G. Michell, Ryuho Kataoka, Takeshi Sakanoi, Daniel K. Whiter, Shin ichiro Oyama, Yasunobu Ogawa, and Satoshi Kurita. Diffuse and Pulsating Aurora. *Space Science Reviews*, 216(1):1–38, 2020. ISSN 15729672. doi: 10.1007/s11214-019-0629-3. URL http://dx.doi.org/10.1007/s11214-019-0629-3.

[9] Fasil Tesema, Noora Partamies, H. Nesse Tyssøy, Antti Kero, and C. Smith-Johnsen. Observations of Electron Precipitation During Pulsating Aurora and Its Chemical Impact. *Journal of Geophysical Research: Space Physics*, 125 (6), 2020. ISSN 21699402. doi: 10.1029/2019JA027713.

[10] A. Pellinen-Wannberg. The EISCAT meteor-head method – a review and recent observations. pages 649–655, 2004.

[11] Markku S Lehtinen and Asko Huuskonen. General incoherent scatter analysis and GUISDAP. *Journal of Atmospheric and Terrestrial Physics*, 58(1):435–452, 1996. ISSN 0021-9169. doi: https://doi.org/10.1016/0021-9169(95)00047-X. URL https://www.sciencedirect.com/science/article/pii/002191699500047X.

[12] Ilkka I. Virtanen, Björn Gustavsson, Anita Aikio, Antti Kero, Kazushi Asamura, and Yasunobu Ogawa. Electron Energy Spectrum and Auroral Power Estimation From Incoherent Scatter Radar Measurements. *Journal of Geophysical Research: Space Physics*, 123(8):6865–6887, 2018. ISSN 21699402. doi: 10.1029/2018JA025636.

[13] Joseph E. Cavanaugh and Andrew A. Neath. The Akaike information criterion: Background, derivation, properties, application, interpretation, and refinements. *Wiley Interdisciplinary Reviews: Computational Statistics*, 11(3):1–11, 2019. ISSN 19390068. doi: 10.1002/wics.1460.

[14] Dieter Bilitza, David Altadill, Yongliang Zhang, Chris Mertens, Vladimir Truhlik, Phil Richards, Lee Anne McKinnell, and Bodo Reinisch. The International Reference Ionosphere 2012 - A model of international collaboration. *Journal of Space Weather and Space Climate*, 4, 2014. ISSN 21157251. doi: 10.1051/swsc/2014004.

[15] Xiaohua Fang, Cora E Randall, Dirk Lummerzheim, Wenbin Wang, Gang Lu, Stanley C Solomon, and Rudy A Frahm. Parameterization of monoenergetic electron impact ionization. 37(November):1–5, 2010. doi: 10.1029/2010GL045406.

[16] J M Picone, A E Hedin, and D P Drob. NRLMSISE-00 empirical model of the atmosphere : Statistical comparisons and scientific issues. 107(1976):1–16, 2002. doi: 10.1029/2002JA009430.

[17] D S Evans and M S Greer. Polar Orbiting environmental satellite space environment monitor - 2 instrument descriptions and archive data documentation. Technical report, 2000.

[18] S. I. Akasofu. The development of the auroral substorm. *Planetary and Space Science*, 12(4):273–282, 1964. ISSN 00320633. doi: 10.1016/0032-0633(64)90151-5.

[19] NOAA. Aurora Tutorial. URL https://www.spaceweather.gov/content/aurora-tutorial.

[20] D. A. Hardy, M. S. Gussenhoven, and R Raistrick. Statistical and Functional Representations of the Pattern of Auroral Energy Flux , Number Flux , and Conductivity. 92, 1987.

[21] E. W. Hones. Transient phenomena in the magnetotail and their relation to substorms. *Space Science Reviews*, 23(3): 393–410, 1979. ISSN 00386308. doi: 10.1007/BF00172247.

[22] Y. Nishimura, J. Bortnik, W. Li, R. M. Thorne, L. R. Lyons, V. Angelopoulos, S. B. Mende, J. W. Bonnell, O. Le Contel, C. Cully, R. Ergun, and U. Auster. Identifying the driver of pulsating aurora. *Science*, 330(6000):81–84, 2010. ISSN 00368075. doi: 10.1126/science.1193186.

[23] Habtamu W. Tesfaw, Ilkka I. Virtanen, and Anita T. Aikio. Characteristics of Auroral Electron Precipitation at Geomagnetic Latitude 67° Over Tromsø. *Journal of Geophysical Research: Space Physics*, 128(7):1–22, 2023. ISSN 21699402. doi: 10.1029/2023JA031382.

[24] S. Kasahara, Y. Miyoshi, S. Yokota, T. Mitani, Y. Kasahara, S. Matsuda, A. Kumamoto, A. Matsuoka, Y. Kazama, H. U. Frey, V. Angelopoulos, S. Kurita, K. Keika, K. Seki, and I. Shinohara. Pulsating aurora from electron scattering by chorus waves. *Nature*, 554(7692):337–340, 2018. ISSN 14764687. doi: 10.1038/nature25505.

[25] Y. Miyoshi, S. Saito, K. Seki, and T. Nishiyama. Relation between fine structure of energy spectra for pulsating aurora electrons and frequency spectra of whistler mode chorus waves. *Journal of Geophysical Research: Space Physics*, pages 1–24, 2015. doi: 10.1002/2015JA021094.Received.

[26] Fasil Tesema, Noora Partamies, Hilde Nesse Tyssøy, and Derek McKay. Observations of precipitation energies during different types of pulsating aurora. *Annales Geophysicae*, 38(6):1191–1202, 2020. ISSN 14320576. doi: 10.5194/angeo-38-1191-2020.

[27] Bing Yang, Emma Spanswick, Jun Liang, Eric Grono, and Eric Donovan. Responses of Different Types of Pulsating Aurora in Cosmic Noise Absorption. *Geophysical Research Letters*, 46(11):5717–5724, 2019. ISSN 19448007. doi: 10.1029/2019GL083289.